Simulation and Experimental Verification of Vibration and Noise Characteristics of Nanocrystalline High-Frequency Transformer

Pengning Zhang, Yajin Yang, Ze Liu, Ning Wang, Chengjian Li, and Jian Zhang

***Abstract*—A high-frequency transformer (HFT) is the core component of a power electronic transformer, but the vibration and noise during normal operation of HFTs are severe. Therefore, this article investigates the vibration noise characteristics of HFT. Firstly, the vibration mechanism of HFT is studied, the electromagnetic force models causing HFT vibration are deduced, and the electromagnetic-mechanical-acoustic multiphysical field coupling model of HFT is established. Then, the vibration and noise characteristics of HFT under the excitation of sinusoidal and square wave are studied and analyzed based on the model. The results show that when the excitation frequency is 5 kHz, the dominant vibration frequency is 10 kHz for sinusoidal excitation. For square wave excitation, the dominant frequencies are 10, 20, and 30 kHz, with a sound pressure of 26.5 Pa, surpassing the 12.9 Pa observed under sinusoidal excitation. Finally, a vibration and noise experimental platform of HFT is built to verify the model, and vibration noise reduction methods for HFT are proposed, including increasing prestress and avoiding the presence of air gaps in the structure. The research results provide a theoretical and experimental basis for the magnetic-mechanical-acoustic multiphysical field coupling and vibration noise reduction of HFTs.**

***Index Terms*—High-frequency transformer (HFT), nanocrystalline core, noise, vibration, vibration reduction.**

I. Introduction

With the development of power electronics technology and the breakthrough of new materials, the power electronic transformer, headed by high frequency, high power and high capacity, has a wide range of applications in the power system [1]. High-frequency transformer (HFT) have become the key component of the transmission channel of distributed power generation system and ac power grid, which has a broad application prospect and is one of the important directions for future development [2].

The main structure of HFT is the core and windings, the core is mainly affected by the magnetostrictive effect and Maxwell stress to produce vibration, and the Lorentz force of the windings is also another cause of HFT vibration [3], [4], [5]. In terms of forecasting methods for conventional transformer vibration and noise, Li et al. and [6] and Lihua et al. [7] realized the numerical calculation of electromagnetic vibration of the transformer by analyzing the energy generalization of the magneto-mechanical coupled system and constructing the J–A hysteresis model of silicon steel sheet. Bouayed et al. [8] used an end-to-end multiphysics modeling solution to predict the vibration and noise radiated by an electrical transformer. At present, the research on vibration and noise in HFT is also developing rapidly. Hsu has studied different amorphous core types in the magnetic field simulation, results suggest that hybrid-type cores have better magnetic properties and lower magnetic losses, but the magnetism in relation to sound level and core vibration is revealed to be difficult to control [9]. Zhang and Li [10] has derived equations for the magnetostriction of amorphous and nanocrystals and pointed out that the vibration noise of HFT under rectangular wave excitation is greater than sinusoidal.

Previously, numerous studies concentrated on vibration and noise reduction in conventional transformers, while theoretical research on HFT in this area is limited. Since the principles of HFT and power transformer are close, the vibration noise reduction analysis of power transformer is available for reference. Girgis et al. [11] found that when the weight of the core was reduced by 10%, the noise of the transformer could be reduced by 9.2 dB. Liu et al. [12] designed an MPP absorber that absorbs specific frequencies and achieved better noise reduction through experimental verification. Liu et al. [13] found that appropriate annealing temperature can improve soft magnetic properties and reduce noise in amorphous alloy strips and cores.

This article takes the vibration noise problem of nanocrystalline core HFT as the research object, builds the electromagnetic-mechanical-acoustic finite element model for the vibration noise calculation under different excitations, and

Received 10 July 2024; revised 29 December 2024; accepted 17 February 2025. Date of publication 26 February 2025; date of current version 14 April 2025. This work was supported in part by the National Natural Science Foundation of China under Grant 52007192, in part by the Fundamental Research Funds for the Central Universities under Grant 2023ZKPYJD09, and in part by the State Grid Corporation of China Headquarters Technology Project under Grant SGAHDK00SPJS2200430. Recommended for publication by Associate Editor M. Duffy. *(Pengning Zhang and Yajin Yang are co-first authors.) (Corresponding author: Yajin Yang)*

Pengning Zhang, Ze Liu, and Ning Wang are with the China University of Mining and Technology(Beijing), Beijing 100083, China (e-mail: zpn2019@cumtb.edu.cn; zqt2300403079@student.cumtb.edu.cn; bqt2200403008@student.cumtb.edu.cn).

Yajin Yang is with Zhejiang University, Hangzhou 310027, China (e-mail: 2010470321@student.cumtb.edu.cn).

Chengjian Li is with the State Grid Sichuan Electric Power Company Ultra High Voltage Branch Ya'an Operation and Maintenance Sub-branch, Ya'an 625000, China (e-mail: licj5770@sc.sgcc.com.cn).

Jian Zhang is with China Electric Power Research Institute, Beijing 100192, China (e-mail: zhangjian3@epri.sgcc.com.cn).

Color versions of one or more figures in this article are available at https://doi.org/10.1109/TPEL.2025.3546063.

Digital Object Identifier 10.1109/TPEL.2025.3546063

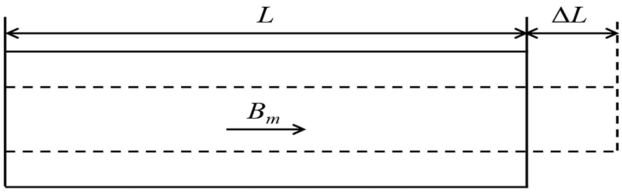

Fig. 1. Schematic diagram of the magnetostrictive effect.

compares it with the experimental data of vibration noise of HFT, verifies the accuracy of the model, and finally puts forward effective methods of vibration and noise reduction of HFT.

II. Theoretical Analysis

A. HFT Vibration Mechanism Analysis

1) Core Vibration Mechanism: The core plays a vital role in the transformer, forming both the path for the magnetic flux to flow through and providing mechanical support for the windings. The operating conditions of HFTs mean that the core material should have a high saturation flux density, low eddy current loss and high magnetic permeability. Therefore, the core of HFTs is often made of amorphous alloys, nanocrystalline alloys, and other new magnetic materials.

The magnetostrictive effect means that under the excitation of the external magnetic field, the shape and size of the material will be deformed to a certain extent. Considering that the volume change of the material is very small, we use linear magnetostriction to model, i.e., as shown in Fig. 1, it is manifested in the elongation or shortening of the material, but the total volume of the material stays unchanged.

For isotropic materials, the magnetostrictive strain is modeled as the following quadratic isotropic form of the magnetization field using tensor notation [14]

$$\boldsymbol{\varepsilon}_{\mathrm{me}} = \frac{3}{2}\frac{\lambda_s}{M_s^2}\mathrm{dev}(\boldsymbol{M}\otimes\boldsymbol{M}) \tag{1}$$

where $\varepsilon_{\mathrm{me}}$ is magnetostrictive strain; M_{s} is saturation magnetization intensity; λ_s is the saturation magnetostriction coefficient; and $\boldsymbol{M}$ is magnetization intensity.

In a magnetic field, the magnetic material and the current-carrying conductor are subjected to magnetic field forces, and we can describe the forces on the core in a magnetic field using the Maxwell stress tensor, which is a surface force, and the magnetic field form of the Maxwell stress tensor in the steady state is shown in the following:

$$\mathbf{T} = \frac{1}{\mu_0}\begin{bmatrix} \left(\mathbf{B}_x^2 - \frac{1}{2|\mathbf{B}|^2}\right) & \mathbf{B}_x\mathbf{B}_y & \mathbf{B}_x\mathbf{B}_z \\ \mathbf{B}_y\mathbf{B}_x & \left(\mathbf{B}_y^2 - \frac{1}{2|\mathbf{B}|^2}\right) & \mathbf{B}_y\mathbf{B}_z \\ \mathbf{B}_z\mathbf{B}_x & \mathbf{B}_z\mathbf{B}_y & \left(\mathbf{B}_z^2 - \frac{1}{2|\mathbf{B}|^2}\right) \end{bmatrix} \tag{2}$$

where $\boldsymbol{T}$ is maxwell stress tensor; $\boldsymbol{B}$ is magnetic flux density; and μ_0 is the permeability of the vacuum.

Since magnetostrictive strain and Maxwell stress are both proportional to the square of the magnetic flux density, the dominant frequency of strain and stress is two times the frequency of the magnetic flux density. When the HFT operates under non-sinusoidal excitation, the spectrum of the vibration will be more complicated, for example, under the square-wave excitation, where the magnetic flux density is mainly the fundamental wave and the third harmonic wave, and the spectrum of the vibration at this time will appear as the two times, four times, and six times the frequency of the excitation frequency.

3) Coil Vibration Mechanism: In a transformer, due to the incomplete nature of magnetic coupling, there is a certain amount of leakage flux in the region around the windings, and the winding current is subjected to the Lorentz force under the action of the leakage flux. Generally speaking, the contribution of Lorentz force to transformer vibration noise is smaller than the contribution of magnetostriction and Maxwell stress to transformer vibration noise. However, because the windings are directly wound on the core of the transformer, the vibration of the core and the windings will be coupled with each other. At the same time, the transformer will produce larger leakage flux in the short-circuit condition or when subjected to larger dc bias, and at this time, the Lorentz force on the windings cannot be ignored. So in order to accurately and comprehensively analyze the vibration noise of the transformer in various operating conditions, it is necessary to analyze the Lorentz force [15].

The expression for the Lorentz force is

$$\mathbf{F} = \int \mathbf{J}\times\mathbf{B}dV \tag{3}$$

where $\boldsymbol{J}$ is the current density.

In the case of winding currents containing harmonics, the frequency components of the Lorentz force will also be more complex, and it is important to avoid damaging the equipment with excessive Lorentz forces from the HFT.

B. HFT Multiphysics Field Coupling Analysis

1) Electromagnetic Field Calculations: Under the excitation of the voltage source, a current is generated in the primary winding of the transformer, and the current excites a magnetic field, of which the majority exists in the core of the nanocrystalline core, and a small portion of the magnetic field passes through the air to form a leakage flux, and, according to the law of electromagnetic induction, the varying magnetic density in the core generates an induced current in the secondary winding.

The governing equations for transient electromagnetic fields are the D'Alembert equations

$$\begin{cases} \nabla^2\mathbf{A} - \mu\varepsilon\frac{\partial^2\mathbf{A}}{\partial t^2} = -\mu\mathbf{J} \\ \nabla^2\phi - \mu\varepsilon\frac{\partial^2\phi}{\partial t^2} = -\frac{\rho}{\varepsilon} \end{cases} \tag{4}$$

where $\boldsymbol{A}$ is magnetic vector potential; ε is conductivity.

2) Mechanical Field Calculations: The equilibrium equation of motion for the mechanical field is as follows:

$$\rho\frac{\partial^2\mathbf{u}}{\partial t^2} + d_a\frac{\partial\mathbf{u}}{\partial t} - \nabla\cdot\boldsymbol{\sigma} = \mathbf{f} \tag{5}$$

where ρ is density; $\boldsymbol{u}$ is displacement; d_a is damping; σ is stress; and $\boldsymbol{f}$ is loading force.

The material's intrinsic relationship is then in accordance with Hooke's law

$$\boldsymbol{\sigma} = \boldsymbol{D}\boldsymbol{\varepsilon} \tag{6}$$

where $\boldsymbol{D}$ is the elastic tensor of the material.

Since there are three unknown quantities, that is, stress, strain and displacement, the coordination equations between strain and displacement need to be supplemented to solve the problem

$$\boldsymbol{\varepsilon} = \frac{1}{2}[(\nabla \mathbf{u})^T + \nabla \mathbf{u}]. \tag{7}$$

3) Acoustic Field Calculations: The acoustic field is solved based on the Helmholtz equation in the frequency domain

$$\nabla \cdot \left(-\frac{1}{\rho}\nabla p\right) - \frac{1}{\rho}\left(\frac{\omega}{c}\right)^2 p = 0 \tag{8}$$

where w is angular frequency and c is the speed of sound in the medium.

The noise of the HFT comes from the vibration of its shell, and the vibration acceleration of the shell is brought into the mechanical-acoustic coupling equation as the source of the sound field

$$-\mathbf{n} \cdot \left(-\frac{1}{\rho}(\nabla p - \mathbf{q_d})\right) = -\mathbf{n} \cdot \mathbf{u_{tt}} \tag{9}$$

where $\boldsymbol{n}$ is the vector perpendicular to the surface; $\boldsymbol{q}_{\mathrm{d}}$ is the dipole domain source; and $\boldsymbol{u}_{tt}$ is the vibration acceleration of HFT.

4) HFT Multiphysics Field Coupling Analysis: In this article, considering that the HFT is mainly subject to nonsinusoidal excitation, the electromagnetic field is analyzed in the time domain, and then the parameters obtained from the electromagnetic field calculations are substituted into the electromagnetic force model to calculate the transient results of the load and external strains to realize the coupling of the mechanical field and the electromagnetic field. Then the vibrational acceleration under the time domain is calculated with the load and strain acting on the mechanical field and the dominant frequency of the vibration is then analyzed in the frequency domain by fast Fourier transform (FFT).

However, due to the special characteristics of the acoustic field, the mesh and the time iteration step can only take a very small value. And if the acoustic field is still analyzed in the time domain, it will bring a great amount of computation, so in this article, after obtaining the dominant frequency of the vibration, the load and the external strains are subjected to the FFT, and the dominant band of HFT vibration signals is swept and analyzed in the mechanically-acoustically coupled field, which saves the time of the solving process. The schematic is shown in Fig. 2, and the final dominant frequency results can be converted by inverse FFT to get the time domain results of the mechanical-acoustic field.

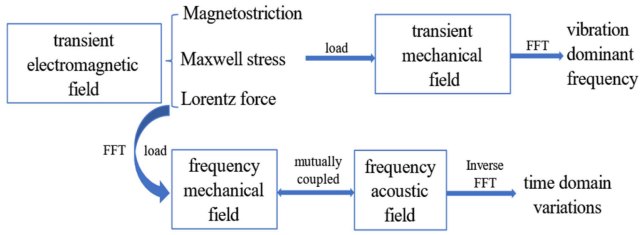

Fig. 2. HFT multiphysics field coupling flowchart.

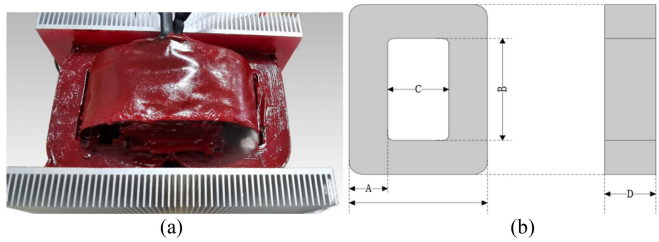

Fig. 3. Shell-type HFT Physical Drawing. (a) HFT physical prototype. (b) Core dimensions.

TABLE I
HFT GEOMETRIC PARAMETER TABLE

Dimensional parameters	Length(mm)
A-core	17
B-window	46
C-window	35
D-strip	43.2
The average length of primary winding	359.23
The average length of secondary winding	243.26
Air gap thickness	0.2

III. MODELING AND SIMULATION

A. Model of Nanocrystalline Iron Core of HFT

To achieve an accurate assessment of HFT vibration and noise, this article presents a multi-physics field modeling of a nanocrystalline shell-type HFT with a rated capacity of 15 kVA and a rated voltage of 760 V based on COMSOL Multiphysics. Shell-type HFT physical diagram is shown in Fig. 3, and the core and winding structure size parameters as given in Table I.

In addition to the core and windings, the HFT also has epoxy resin, connectors, and some smaller ancillary structure components. So, in this article, the following simplification principles are used to simplify the geometric structure in 3D modeling.

1) Use the equivalent winding to replace the actual primary/secondary winding, this operation can avoid the complex structure of the multi-turn coil for 3D modeling.
2) Ignore some smaller connectors between the core and the windings and the pads between the primary and secondary windings.

In this article, two different sets of geometries are used to model different physical fields, as shown in Fig. 4, Geometry 1 and geometry 2. Geometry 1 applies to the calculation of electromagnetic fields, and considering that the permeability of other parts such as the heat sink is similar to that of air, only the core, winding and air domains are modeled. However, when analyzing the mechanical-acoustic field, the structure of epoxy, core connectors, and heat sinks will affect the vibration so that in the geometry must be considered comprehensively when studying vibration noise. Using the symmetry of the model, the

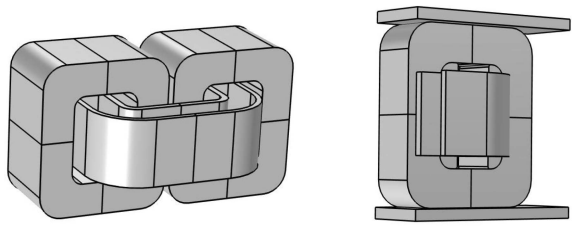

Fig. 4. Geometry 1 and Geometry 2. (a) Geometry 1. (b) Geometry 2.

TABLE II
HFT MAGNETIC CHARACTERISTICS PARAMETER TABLE

component	permeability	conductivity(S/m)
core	B-H curve	--
coil	1	1.85×10^{7}

TABLE III
CIRCUIT PARAMETER TABLE

Parameter	value
rated voltage	760 V
rated capacity	15kVA
rated frequency	5 kHz
primary winding turns	28
Secondary winding turns	28

model was sliced into one-fourth to simplify the calculations. The mapping of physical quantities between the two geometries is realized through the generalized stretching operator.

B. Magnetization Characteristics and Mechanical Property Parameters of HFT

Because of the fine grain structure and low anisotropy of nanocrystalline alloys, the nanocrystalline materials are regarded as isotropic materials in the magnetic field model. And the hysteresis effect of nanocrystalline cores can be neglected considering that the hysteresis return of materials is very narrow, so the basic magnetization curves are used instead of hysteresis return for modeling. The magnetic parameters of each component of the HFT are given in Table II.

However, the original nanocrystalline magnetization data contains some ripples that do not conform to the actual physical situation, and the existence of ripples will lead to instability in numerical calculations, which will result in a longer calculation time, and even failure to converge. So, the original data must be subjected to a certain degree of smoothing. In this article, we adopt the simultaneous exponential extrapolation (SEE) method proposed in [16], which fully considers the physical properties of magnetic saturation and extrapolates the magnetization curves in the magnetically saturated region, and eliminates the unreasonable ripples of the *B–H* curves, thus improving the convergence of the model. Fig. 5 shows the original *B–H* curve and the optimized curve using SEE.

The circuit parameter of the HFT is given in Table III.

After completing the solution of the electromagnetic field, the corresponding magnetostrictive strain, Maxwell stress and

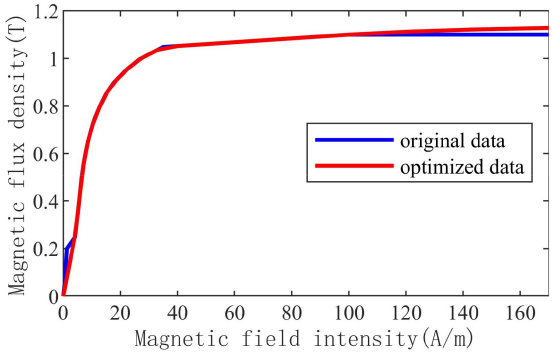

Fig. 5. *B–H* curve original and optimized data.

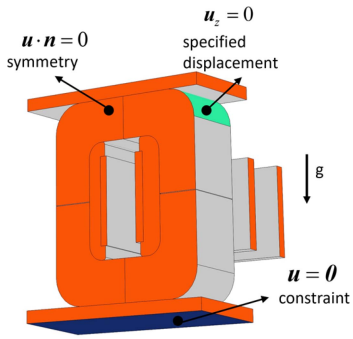

Fig. 6. Mechanical field boundary condition setting.

TABLE IV
MECHANICAL FIELD PARAMETER TABLE

Component	Material	Density (kg/m^3)	Young's modulus(Gpa)
core	nanocrystalline	7180	150
coil	copper	8940	126
insulating varnish	epoxy resin	1673	10.4
heat sinks	aluminum	2700	70

Lorentz force densities can be obtained. Then, the magnetostrictive strain is taken as the external strain of the core, Maxwell stress as the surface load on the core surface, and Lorentz force as the body load on the windings, considering the gravitational force and external constraints imposed on the transformer during its actual operation as shown in Fig. 6. Assigning the values of the mechanical properties of the material as given in Table IV, the distribution of the mechanical field of the HFT can be obtained.

When simulating the vibration noise of HFT, it is often desired to analyze it in an infinite spatial domain, so as to avoid the sound wave reflecting at the boundary, which will affect the analysis of the noise. But if the solution domain is set too large, it will consume the computational resources greatly and reduce the efficiency of the solution. In this article, a perfect-matched layer (PML) is used to achieve this purpose. The PML is a numerical simulation method to make the energy of the wave fully absorbed in the domain of the layer, and an accurate approximation of the free space can be realized through the PML.

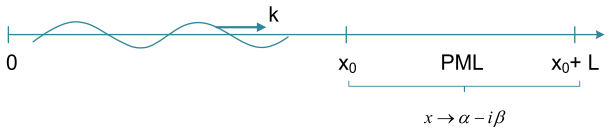

Fig. 7. Schematic Diagram of PML Principle.

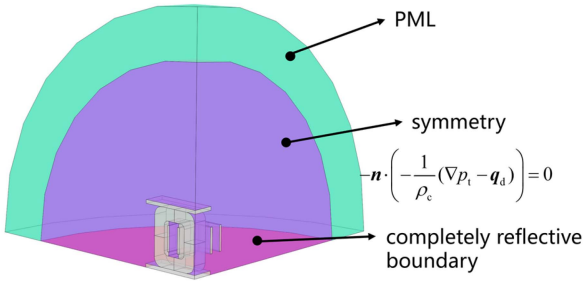

Fig. 8. Acoustic field boundary condition setting.

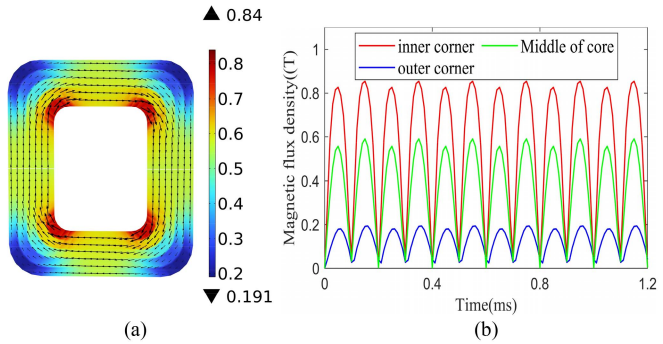

Fig. 9. HFT Magnetic Flux Density. (a) Core distribution. (b) Variation over time.

The basic idea of the PML is shown in Fig. 7, the coordinates are transformed to the complex domain, and the imaginary part β denotes the attenuation coefficient, which makes the energy of the wave attenuated and absorbed before it reaches the end of the PML, x_0+L, by choosing a suitable function of α and β.

Since the acoustic impedance of the ground is much larger than that of the air, the ground is set as a completely reflective boundary, and the boundary conditions of the acoustic field are set as shown in Fig. 8. The PML acts on the outermost part of the solution domain.

C. Calculation Results

Based on COMSOL to calculate the electromagnetic field characteristics of the HFT at rated operating conditions. The excitation is applied through an external circuit voltage source, and a sinusoidal source and a square wave source are successively applied to the HFT, both at a frequency of 5 kHz, and the solution time is set to six cycles, i.e., 0.0012 s.

The magnetic flux density of the core peaks at $t = 0.00015$ s. At this time, the magnetic flux density map of the xz section of the core of the HFT and the magnetic densities at the inner corners, outer corners, and air gap are shown in Fig. 9. The magnetic

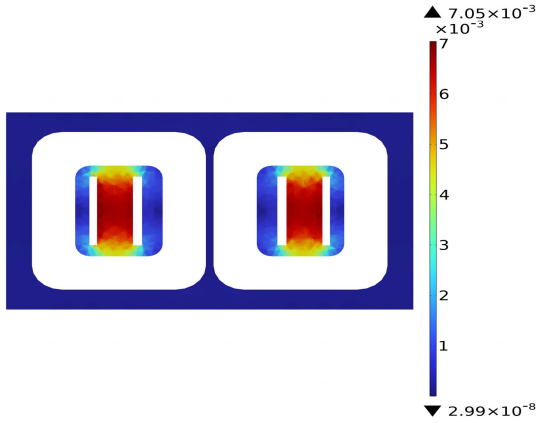

Fig. 10. Air domain leakage flux distribution.

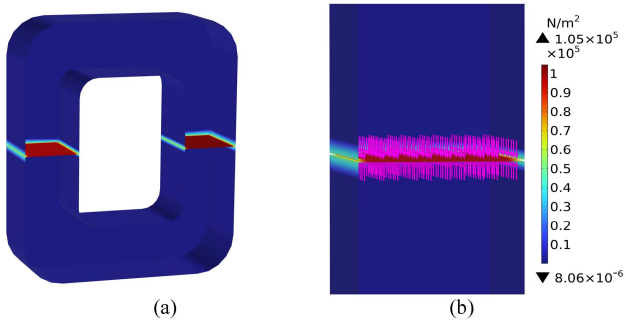

Fig. 11. Maxwell's stress. (a) Overall maxwell stress distribution in Core. (b) Magnified maxwell stress distribution in air gap.

density is maximum at the inner corners and minimum at the outer corners.

The leakage flux in the air domain is the direct cause of the Lorentz force in the windings; to understand the distribution of the magnetic flux in the air domain except for the air gap, this article plots the distribution of the leakage flux in the air domain at $t = 0.0015$ s. As shown in Fig. 10, the leakage flux is mainly distributed in the air domain surrounded by the core, and the leakage flux existing in the air domain outside of the core is very small, in which the leakage flux between the primary and secondary windings is the largest.

Since the Maxwell stress mainly acts on the interfaces of the two media, and the magnetic permeability of the core is much larger than that of the air, the Maxwell stress is mainly concentrated in the air gap region, as shown in Fig. 11. The maximum value reaches 9.29×10^4 Pa, and the direction of the stress is such that the upper and lower parts of the core are attracted to each other. The size is uniformly distributed in the air gap region. Maxwell stress is a significant contributor to HFT vibration after the air gap is opened.

The results of the x, y, and z components of the magnetostrictive strain are shown in Fig. 12(a), it can be found that all three components are the largest strain in the inner corner, this is because the magnetic flux density is the largest in the inner corner, the magnetostrictive strain is proportional to the square of the magnetic flux density. At the same time, the upper yoke and the lower yoke have a larger value of the strain in the x-

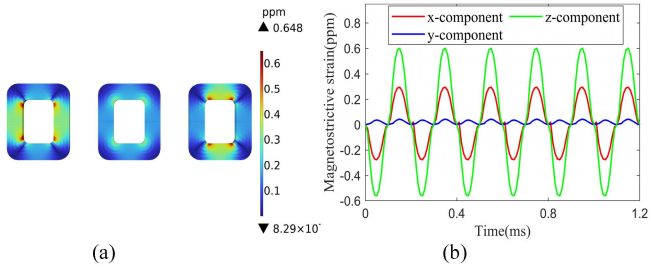

Fig. 12. HFT Magnetostrictive Strain. (a) Strain distribution (x, y, z). (b) Strain variation over time (x, y, z).

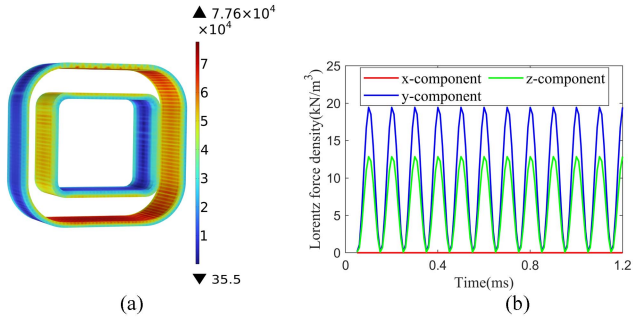

Fig. 13. HFT Lorentz Force Density. (a) Windings distribution. (b) Time variation (x, y, z).

and y-direction, and the left and right sides of the core have a larger value of the strain in the y, z direction. The strain at a point in the inner corner is plotted as shown in Fig. 12(b), the magnetostrictive strain is a periodic change of 10 kHz, which is two times the rated frequency.

The Lorentz force density of the winding is shown in Fig. 13(a), in the inner part of the primary winding and the outer part of the secondary winding, there is a large Lorentz force density, in which the maximum value reaches 7.76×10^4 N/m^3, this is because the leakage flux is the largest in the air domain of the primary and secondary windings. And the Lorentz force density is uniformly distributed along the direction of current flow. Fig. 13(b) plotted at a point in the primary winding by the Lorentz force density of the x, y, and z component, y- and z-direction of the Lorentz force density is much greater than the x direction, and the frequency of Lorentz force is 10 kHz.

The obtained loads and strains are applied to the HFT in the time domain to solve the vibration. The vibration acceleration of an object is a measure of vibration and noise radiation. To better understand the frequency components of the vibration acceleration, the vibration results under sinusoidal and square wave excitation are converted from the time domain to the frequency domain using FFT as shown in Fig. 14. It can be seen that the dominant frequency of the HFT vibrational acceleration under sinusoidal excitation is 10 kHz, while the dominant frequencies of the vibrational acceleration under square wave excitation are 10, 20, and 30 kHz.

The amplitude and phase of the load and external strain at the dominant frequency are obtained by FFT. The loads and external strains in the frequency domain are applied to the mechanical-acoustic coupled field model, and the vibration displacement

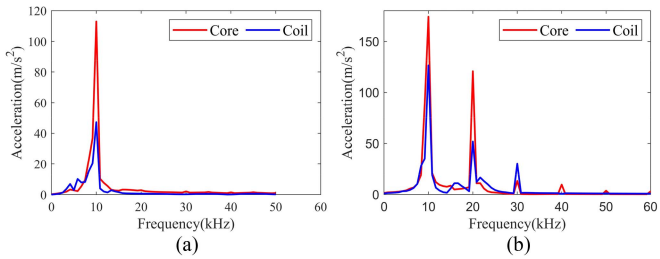

Fig. 14. HFT vibration dominant frequency analysis. (a) Under sinusoidal excitation. (b) Under square excitation.

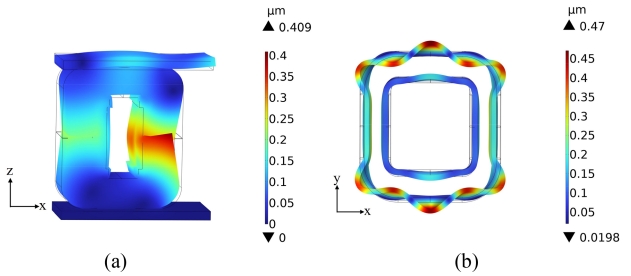

Fig. 15. Vibration displacement at 10 kHz under sinusoidal excitation. (a) Core. (b) Windings.

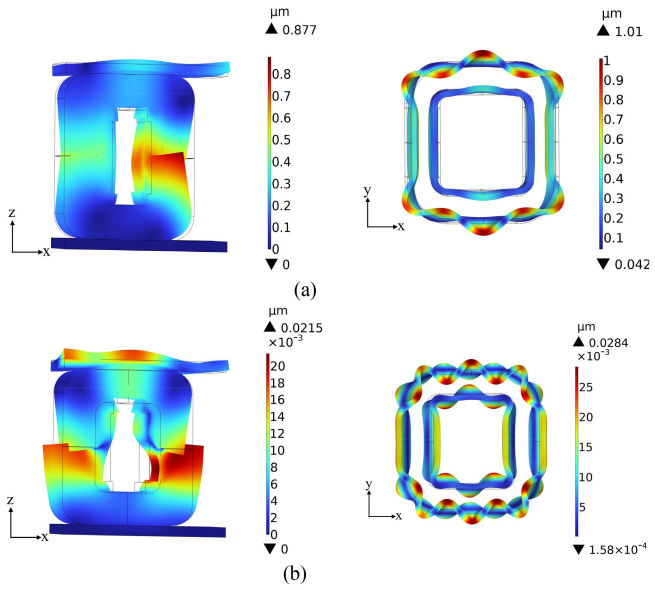

Fig. 16. Vibration displacement plots at 10 and 20 kHz under square wave excitation. (a) 10 kHz. (b) 20 kHz.

diagrams for the dominant frequencies of sinusoidal excitation and square wave excitation are calculated as shown in Figs 15 and 16.

It can be seen that the vibration pattern of 10 kHz is that the core is squeezed in the x-direction, and due to the superposition of Maxwell's stress and magnetostrictive strain at the air gap, it results in the core in the air gap region having a maximum displacement of 0.409 μm, and the cores near the air gap region are close to each other under the action of Maxwell's stress. The heat sinks at the top of the core is also slightly deformed due to

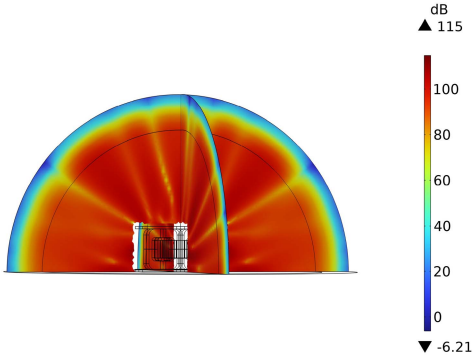

Fig. 17. Acoustic field distribution under sinusoidal excitation.

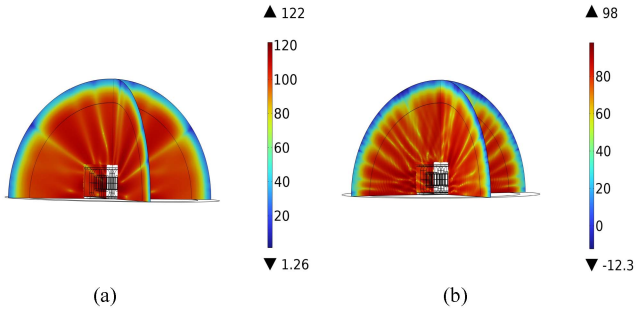

Fig. 18. Acoustic field distribution under square wave excitation. (a) 10 kHz. (b) 20 kHz.

the influence of the core. The primary and secondary windings are close to each other in the x-direction under the action of the Lorentz force, and both windings show different degrees of distorted wave-like deformation in the y-direction, and the displacement of the primary winding is larger than that of the secondary winding, with the maximum displacement 0.47 μm.

The vibration pattern at 10 kHz under square wave excitation is the same as for sinusoidal excitation, but the maximum displacements of the core and windings reach 0.88 and 1 μm. The vibration pattern under the frequency component of 20 kHz is that the upper part of the core compresses inwardly and the lower part stretches outwardly, the upper radiator exhibits wave-like deformation, and the upper and lower sides of the primary and secondary windings exhibit more complicated twisting deformation concerning 10 kHz, and the maximum displacements of the core and windings reach 0.0215 and 0.0284 μm, respectively.

The HFT near-field noise calculation results are shown in Figs 17 and 18. The maximum sound pressure (SP) under sinusoidal excitation reaches 115 dB. While the noise under square wave excitation is larger than the noise generated by sinusoidal excitation, the noise in the air domain is 122 dB maximum at 10 kHz and 98 dB maximum at 20 kHz. Moreover, the SP distribution is symmetric about the transformer and spreads from the HFT surface to the surroundings and decreases gradually, which is in line with the trend of SP distribution. The attenuation in the setup of the PML is close to 0, which indicates that the PML plays a role in attenuating and absorbing the noise.

In order to understand more intuitively the rule of change of vibration and noise signals with time, this article uses the inverse

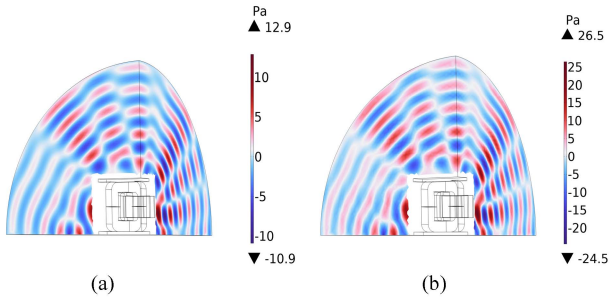

Fig. 19. HFT sound pressure time-domain distribution. (a) SP under sinusoidal excitation. (b) SP under square excitation.

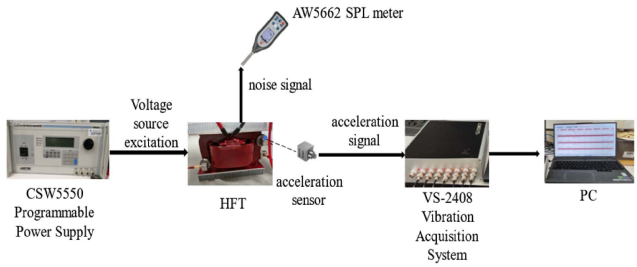

Fig. 20. Setup for vibration and acoustic noise measurement platform.

FFT to convert the signals back to the time domain. Fig. 19 gives the SP field distribution around the transformer under the square wave and sinusoidal excitation at the same moment, after the transformer vibration, through the vibration transfer between the air molecules, so that the acoustic wave propagates in the air. In Fig. 19, we can see the clear peaks, troughs and knots, and the acoustic wave energy with the increase of the propagation distance. The maximum value of the SP under the square wave excitation is 26.5 Pa, the maximum SP in the air domain under sinusoidal excitation is only 12.9 Pa.

IV. Analysis of Experimental Results

A. Experimental Analysis of Core Vibration

To verify the correctness of the above calculation results, this article builds the HFT vibration noise experimental measurement platform, as shown in Fig. 20. Generating sine and square wave excitation with the CSW5550 programmable power supply, and the vibration characteristics of the nanocrystalline core are measured by the WA0101 uniaxial acceleration sensor adsorbed on the core surface, and the vibration signals are connected to the VS-2408 vibration data acquisition platform for acquisition. For noise measurements, an AWA5662 multifunctional sound level meter is used with a Z-weighted sound level range of 25–140 dB, which is transmitted to a PC via a USB cable for processing.

B. Experimental Results

A sinusoidal voltage excitation of 50, 150, and 250 V has been applied to the HFT at a frequency of 5 kHz, acceleration measurement points were arranged on the front and side of the

TABLE V
COMPARISON OF EXPERIMENTAL AND SIMULATED VALUES OF SINUSOIDALLY EXCITED ACCELERATION

Point	Acceleration/m·s^{-2}					
	50V		150V		250V	
	Measurement	Simulation	Measurement	Simulation	Measurement	Simulation
A1	5.4	4.78	42.4	43	101.0	141
A2	5.6	3.7	47.6	36	100.4	101.3
A3	2.7	2.49	19.88	19.4	36.7	42.1

TABLE VI
EXPERIMENTAL AND SIMULATED VALUES OF SPL WITH SINUSOIDAL EXCITATION

voltage/V	Measured value /dB	Simulated value/dB	error/%
50	49.1	45.36	7.6
150	68.2	64.44	5.51
250	72.7	73.3	0.83

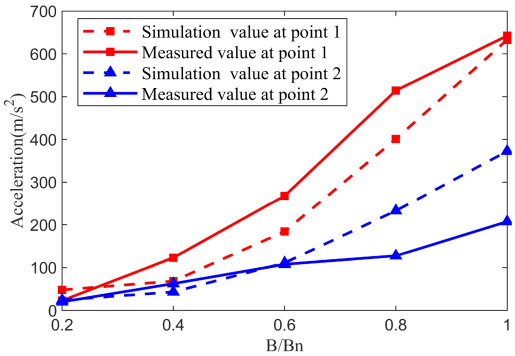

Fig. 21. Comparison of simulated and experimental values of vibration acceleration under square wave excitation.

TABLE VII
COMPARISON OF SIMULATED AND EXPERIMENTAL VALUES OF SOUND PRESSURE LEVEL UNDER SQUARE WAVE EXCITATION

voltage/V	SPL/dB			
	Measured value at point 1	Simulated value at point 1	Measured value at point 2	Simulated value at point 2
140	73.1	69.51	78.1	69.91
280	75.3	72.61	79.1	74.19
420	76.2	77.89	83.2	79.88
560	77.3	87.94	86.6	89.04
700	79.5	91.92	92.9	93.10

TABLE VIII
EFFECT OF AIR GAP LENGTH ON LINE-AVERAGED SPL OF HFT CONTOUR LINE

Air Gap Length (mm)	SPL(dB)
0	68.26
0.2	93.88

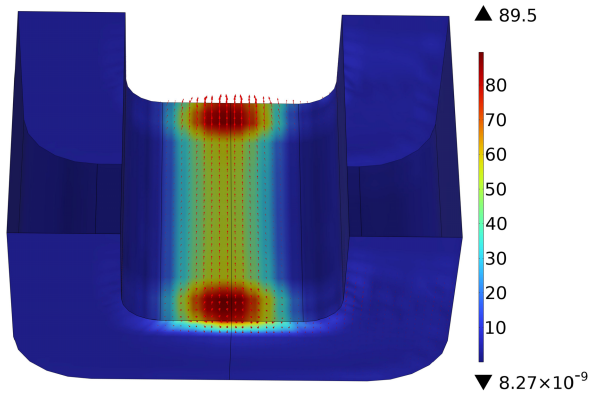

Fig. 22. Maxwell stress distribution in core without air gap.

HFT core, and SP level measurement points were arranged on the contour line of the HFT.

The experimental and simulated values of vibration acceleration under sinusoidal excitation are shown in Table V, and the relative error is 15.18%.

Combining the HFT and the actual situation of the test site, a line 0.3 m from the body and one-two the height of the transformer from the ground is selected as the contour line in this article. The background noise of the test site is 41.6 dB, and since the SP level of the transformer is at least 10 dB higher than the background noise during the measurement, there is no need to correct the results for the background noise. SPL measurement results are presented in Table VI. The relative error in SPL is 4.65%.

A square wave voltage with a frequency of 5 kHz and voltages of 140, 280, 420, 560, and 700 V is applied to the transformer in turn. The relationship between the measured and simulated values of acceleration and magnetic density is plotted in Fig. 21. It can be seen that the simulated and measured values of acceleration show good consistency and agreement. The comparison between the experimental and simulated values of SP level under square wave excitation is given in Table VII. Measurement point 1 is on the contour line directly in front of the HFT and measurement point 2 is on the contour line to the side of the HFT. The relative error is 6.38%, which indicates the correctness of the model.

V. ANALYSIS OF HFT VIBRATION AND NOISE REDUCTION MEASURES

A. *Effect of Air Gap Length on HFT Vibration Noise*

In order to facilitate the processing of windings, an air gap is often opened in the middle of the core of the HFT, and the effect of whether or not to open the air gap on the vibration noise is analyzed in this section.

The core does not open the air gap, as shown in Fig. 22, Maxwell stress maximum appeared in the upper and lower iron yoke, and the maximum Maxwell stress for 89.5 Pa, the value is very small, can be ignored. But in the opening of the air gap, as shown in Fig. 11, Maxwell stress of the maximum value appeared in the air gap, the maximum value reaches 9.29×10^4 Pa.

As shown in Table VIII, the line-averaged SPL of the contour line increased by 25.62 dB after a 0.2 mm air gap was opened.

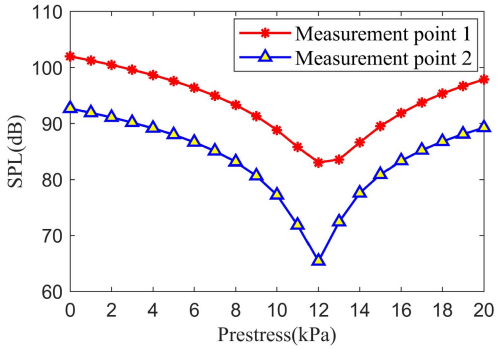

Fig. 23. SPL vs. core prestressing.

B. Effect of Different Core Prestressing on Vibration Noise of HFT

The outer surface of the U-shaped core is usually wrapped with a steel strip, which provides a certain amount of prestress, and serves to impede the vibration of the core. But as the prestress increases, the magnetostrictive coefficient of the core also increases, so theoretically there exists an optimal size of the pre-stress, and the vibration noise of the core can be minimized [17].

The prestress load with a minimum value of 0, a maximum value of 20 kPa and a step size of 1 kPa are applied sequentially on the outer surface of the core, and the results obtained are shown in Fig. 23. It can be seen in the range of 0 to 12 kPa, the SPL of the noise decreases by close to 1 dB for every increase of 1 kPa of prestress, and the noise reaches the minimum value when the applied prestress is 12 kPa, which is a decrease of 18.98 dB compared with no applied prestress load. But if the prestress is greater than 12 kPa, the SPL increases and is even greater than the SPL when no prestress load is applied.

VI. Conclusion

In this article, the vibration and noise characteristics of a nanocrystalline HFT have been thoroughly investigated through both simulation and experimental verification. The conclusions are as follows.

1) Under sinusoidal excitation at a frequency of 5 kHz, the dominant vibration frequency of the HFT is 10 kHz. In contrast, for square wave excitation, the dominant frequencies are 10, 20, and 30 kHz, with a maximum SP of 26.5 Pa, which surpasses the 12.9 Pa observed under sinusoidal excitation.
2) The experimental results showed good consistency with the simulated values, with relative errors of 15.18%, 4.15% and 6.38% for vibration acceleration and SP level, respectively, under sinusoidal and square wave excitations.
3) The effects of air gap length and core prestressing are analyzed. The presence of an air gap in the core structure exacerbates vibration noise, while an optimal level of core prestressing can help minimize vibration noise.

References

[1] H. Fan and H. Li, "High-frequency transformer isolated bidirectional DC–DC converter modules with high efficiency over wide load range for 20 kVA solid-state transformer," *IEEE Trans. Power Electron.*, vol. 26, no. 12, pp. 3599–3608, Dec. 2011.
[2] M. S. Sanjari Nia, P. Shamsi, and M. Ferdowsi, "Investigation of various transformer topologies for HF isolation applications," *IEEE Trans. Plasma Sci.*, vol. 48, no. 2, pp. 512–521, Feb. 2020,.
[3] P. Shuai and J. Biela, "Influence of material properties and geometric shape of magnetic cores on acoustic noise emission of medium-frequency transformers," *IEEE Trans. Power Electron.*, vol. 32, no. 10, pp. 7916–7931, Oct. 2017.
[4] K.-Y. Yoo, B. K. Lee, and D.-H. Kim, "Investigation of vibration and acoustic noise emission of powder core inductors," *IEEE Trans. Power Electron.*, vol. 34, no. 4, pp. 3633–3645, Apr. 2019.
[5] B. X. Du and D. S. Liu, "Dynamic behavior of magnetostriction-induced vibration and noise of amorphous alloy cores," *IEEE Trans. Magn.*, vol. 51, no. 4, Apr. 2015, Art. no. 7208708.
[6] Y. Li, Y. Li, J. Zhu, L. Zhu, and C. Liu, "Vibration estimation in power transformers based on dynamic magnetostriction model and finite-element analysis," *IEEE Trans. Appl. Supercond.*, vol. 31, no. 8, Nov. 2021, Art. no. 5500904.
[7] Z. Lihua, L. Jingjing, Y. Qingxin, Z. Jianguo, and C.-S. Koh, "An improved magnetostriction model for electrical steel sheet based on jiles–atherton model," *IEEE Trans. Magn.*, vol. 56, no. 3, Mar. 2020, Art. no. 7514604.
[8] K. Bouayed, L. Mebarek, V. Lanfranchi, J.-D. Chazot, R. Marechal, and M.-A. Hamdi, "Noise and vibration of a power transformer under an electrical excitation," *Appl. Acoust.*, vol. 128, pp. 64–70, Dec. 2017.
[9] C.-H. Hsu, M.-F. Hsieh, C.-M. Fu, and Y.-M. Huang, "Effects of multicore structure on magnetic losses and magnetomechanical vibration at high frequencies," *IEEE Trans. Magn.*, vol. 51, no. 11, Nov. 2015, Art. no. 8402704.
[10] P. Zhang and L. Li, "Vibration and noise characteristics of high-frequency amorphous transformer under sinusoidal and non-sinusoidal voltage excitation," *Int. J. Elect. Power Energy Syst.*, vol. 123, Dec. 2020, Art. no. 106298.
[11] R. S. Girgis, M. S. Bernesjo, S. Thomas, J. Anger, D. Chu, and H. R. Moore, "Development of ultra-low-noise transformer technology," *IEEE Trans. Power Del.*, vol. 26, no. 1, pp. 228–234, Jan. 2011.
[12] D. Liu, B. Du, M. Yan, and S. Wang, "Suppressing noise for an HTS amorphous metal core transformer by using microperforated panel absorber," *IEEE Trans. Appl. Supercond.*, vol. 26, no. 7, Oct. 2016, Art. no. 5501205.
[13] D. Liu, J. Li, R. K. Noubissi, S. Wang, X. Xu, and Q. Liu, "Magnetic properties and vibration characteristics of amorphous alloy strip and its combination," *IET Elect. Power Appl.*, vol. 13, no. 10, pp. 1589–1597, Oct. 2019.
[14] X. Liu and X. Zheng, "A nonlinear constitutive model for magnetostrictive materials," *ACTA MECH SINICA*, vol. 21, no. 3, pp. 278–285, Jun. 2005.
[15] F. Zhang, S. Ji, H. Ma, and T. K. Saha, "Operational modal analysis of transformer windings," *IEEE Trans. Power Del.*, vol. 35, no. 3, pp. 1285–1298, Jun. 2020.
[16] D. K. Rao and V. Kuptsov, "Effective use of magnetization data in the design of electric machines with overfluxed regions," *IEEE Trans. Magn.*, vol. 51, no. 7, Jul. 2015, Art. no. 6100709.
[17] Y. Du, M. Wu, L. Zhao, G. Wang, C. Qiao, and Y. Chen, "Correlation analysis between noise and operating parameters of transformers with different rated capacities," in *Proc. IEEE 4th China Int. Youth Conf. Elect. Eng.*, Dec. 2023, pp. 1–5.

Pengning Zhang was born in Yantai, China, in 1991. He received the Ph.D. degree in electrical engineering from the North China Electric Power University, Beijing, China, in 2019.

He has been an Associate Professor with School of Mechanical Electronic and Information Engineering, China University of Mining and Technology, Beijing, China, since 2019. His research interests include research on electromagnetic, vibration, and noise analysis on electromagnetic equipment.

Yajin Yang was born in Shanxi, China, in 2003. He received the B.S. degree in electrical engineering from China university of mining and technology-Beijing, Beijing, China, in 2024. He is currently working toward the master's degree in electrical engineering with Zhejiang University, Hangzhou, China.

His research interests include high-frequency transformer and multi-physics coupling.

Ze Liu was born in Shandong, China, in 2000. He received the B.S. degree in electrical engineering from Tianjin Polytechnic University, Tianjin, China, in 2023. He is currently working toward the master degree in electrical engineering with China University of Mining and Technology-Beijing, Beijing, China.

His research interests lie in high-frequency transformer optimization design and simulation.

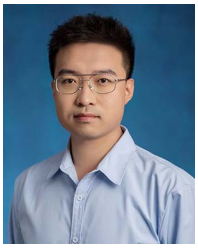

Ning Wang was born in Jinzhong, China, in 1994. He received the M.S. degree in electrical engineering from the Liaoning Technical University, Liaoning, in 2022. He is currently working toward the Ph.D. degree in electrical engineering with the School of Mechanical Electronic and Information Engineering, China University of Mining and Technology, Beijing, China.

His current research interests include magnetic materials and high-frequency transformer.

Chengjian Li was born in Chongqing, China, in 1991. He received the bachelor's degree in civil engineering (power transmission direction) from Northeast Electric Power University, Jilin City, China, in 2014.

After the graduation, he joined the Ultra-High Voltage Branch of State Grid Sichuan Electric Power Company. His area of responsibility is the transmission line.

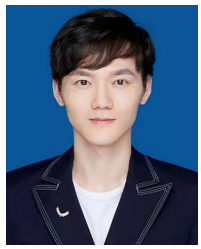

Jian Zhang is currently a Senior Engineer with China Electric Power Research Institute, is proficient in transformer internal structures, production processes, electric field calculations, and insulation levels. He received the Ph.D. degree in electrical engineering from the North China Electric Power University, Beijing, in 2020. He explores digital twin models and failure causes, offering design suggestions.